

Three-Dimensional Porous Structures of CO₂-Induced Salt Precipitation Sustaining Halite Self-Enhancing Growth

Mohammad Nooraiepour,^{1*} Mohammad Masoudi,^{1,2} Hannelore Derluyn,³ Pascale Senechal,⁴ Peter Moonen^{3,4} and Helge Hellevang¹

¹ Department of Geosciences, University of Oslo, P.O. Box 1047 Blindern, 0316, Oslo, Norway.

² Applied Geoscience Department, SINTEF Industry, 7465, Trondheim, Norway.

³ Universite de Pau et des Pays de l'Adour, E2S UPPA, CNRS, LFCR, Pau, France.

⁴ Universite de Pau et des Pays de l'Adour, E2S UPPA, CNRS, DMEX, Pau, France.

Corresponding author: mohammad.nooraiepour@geo.uio.no

Abstract

Salt precipitation during CO₂ storage in saline aquifers presents challenges for injectivity and containment, with broader implications for soil salinization and cultural heritage preservation. This study utilizes time-lapse X-ray and spectral micro-computed tomography, scanning electron microscopy, and deep learning-assisted image analysis to investigate halite crystallization and brine consumption in porous medium. We identified three-dimensional halite growth structures functioning as a secondary porous medium. Visualizing the spatio-temporal dynamics of salt-brine coexistence and halite precipitation revealed critical insights into the self-enhancing nature of salt growth. Expanding gas-liquid contact surfaces and initial crystal nucleation sites significantly enhanced evaporation and growth rates. Hydrophilic halite crystals attract brine films, establishing a feedback loop that perpetuates growth. The encapsulation of brine between grain surfaces and umbrella-like salt crusts was observed. Delineating the self-enhancing growth, including the role of capillary forces and surface-interface processes, is crucial for improving CO₂ injection efficiency and integrity, as well as for addressing environmental challenges related to soil salinization.

Keywords: Salt Precipitation; Saline Aquifer; Mineral Growth; Porous Media; CO₂ Storage

Significance Statement

Salt precipitation in porous materials impacts CO₂ storage, soil salinization, cultural heritage preservation, and infrastructure durability. This study characterizes brine evaporation and halite crystal growth in porous media using high-resolution timelapse X-ray tomography, spectral imaging, and electron microscopy. We reveal halite structures forming a secondary porous geometry, with two key impacts: 1) demonstrating brine-salt phase coexistence through characterization of self-enhancing halite growth, enabling better understanding of crystallization and mitigation strategies; 2) evaluating assumptions and identifying critical gaps in parameters governing evaporation-precipitation processes, essential for improved predictive modeling. These findings advance knowledge of salt crystallization dynamics and inform strategies for engineering and environmental applications.

Introduction

Global efforts to combat climate change increasingly target greenhouse gas emissions, particularly carbon dioxide (CO₂). The European Union (EU) aims to achieve climate neutrality by 2050 (1), emphasizing large-scale Carbon Capture and Storage (CCS) deployment (2). Meeting these goals requires rapid expansion of CO₂ injection facilities across the European Economic Area. By 2040, an annual capacity of 250 million tonnes of CO₂ is needed, with an interim target of 50 million tonnes by 2030 (2). This demands approximately 100 injection wells by 2030—each at 0.5 Mtpa—requiring one well every three weeks, escalating to one per week by 2040, even with high-performance wells at 1 Mtpa.

Efficient injectivity is critical for large-scale CCS, enabling CO₂ to flow through reservoir rocks. Injecting supercritical CO₂ (scCO₂) into geological formations at millions of tonnes annually, when undersaturated with water, evaporates in-situ brine, concentrating dissolved salts (3–5). This triggers salt precipitation in porous

media when solubility limits are exceeded under reservoir conditions, potentially clogging pores, reducing permeability, and increasing pressure near the injection well (6–9). In high-salinity aquifers, these effects can impair CO₂ storage performance, injectivity, and containment (10–15). Economically, salt precipitation incurs significant costs, requiring remedial actions or halting injection (16).

In hypersaline aquifers, CO₂-induced salt precipitation escalates due to complex physicochemical fluid-rock interactions. Globally, several CCS reservoirs exhibit high salinity: Snøhvit (Barents Sea, Norway) exceeds 100,000 parts per million (ppm) Endurance (North Sea, UK) surpasses 250,000 ppm (17); Quest (Canada) exceeds 270,000 ppm NaCl equivalent (18, 19). Ketzin (Germany) reaches 230,000 ppm total dissolved solids (TDS) (8, 20); Illinois Basin-Decatur (USA) approximates 200,000 ppm TDS (21, 22); Aquistore (Saskatchewan, Canada) hits 330,000 ppm TDS (7); and Greensand (Denmark) potentially exceeds 100,000 ppm TDS (23). These high-salinity settings challenge CO₂ storage but are critical for global emission reduction efforts.

Salt crystallization in porous media extends beyond CO₂ sequestration, affecting diverse environmental and engineering fields. In soil mechanics, it alters structure and fertility, causing salinization (24, 25). In agriculture, salt accumulation reduces crop yields and soil health, necessitating advanced management (24). In evaporation processes, it modifies drying kinetics in saturated media like food, impacting quality and stability (26, 27). In construction, salt crystallization via efflorescence (surface) or subflorescence (subsurface) damages building materials and cultural heritage, sourced from rainwater, groundwater, marine spray, or deicing salts (28–32), detrimental to aesthetics and mechanical integrity. Low humidity accelerates surface crusting, hindering evaporation, while higher humidity promotes subsurface precipitation, sustaining conductivity and evaporation (24, 33). Environmental cycles, like wetting-drying, exacerbate deterioration (34–36), highlighting the need for advanced preservation research.

Although experimental, numerical, and theoretical studies on carbon sequestration in saline aquifers have focused on predicting salt precipitation's amount and location (3–5), less attention has addressed the physics of precipitation, growth structures, and dynamics at the fluid-solid interface near the evaporation/precipitation front. These studies often overlook in-situ brine availability and aggregation structures, which critically shape crystallization dynamics and morphology by ensuring continuous solute transport from the brine source.

To explore salt's self-enhancing growth via three-dimensional structures nucleating on secondary substrates (prior crystals) (37, 38) and brine film continuity, we investigate CO₂-induced salt precipitation in porous media with ensured brine availability during evaporation-precipitation experiments. High-resolution imaging reveals halite aggregates forming secondary porous structures within the original medium. This study highlights the broader significance of understanding salt crystallization's self-enhancing dynamics, addressing these complex challenges.

Results

Brine-salt coexistence and crystallization-aggregation behavior

Figure 1 depicts three spatiotemporal stages (t₁–t₃, consecutive days) of residual brine saturation and salt precipitation in a porous medium, with xz/yz cross-sections showing vertical brine-salt distribution and xy views detailing horizontal profiles along the flow cell's height (subfigures B–D zoom from A's yellow/blue regions). This illustrates halite crystallization and aggregation with active gravitational forces.

CO₂ injection displaces brine via viscous two-phase flow, with ongoing gas movement driving evaporation of residual brine water, regulated by brine-CO₂ solubility under experimental conditions. The gas-brine interface, shaped by hydrophilic glass beads and halite (Fig. 1, xy views), forms distinct menisci. The aqueous phase coats beads and crystals, clustering residual brine and enhancing wetting-phase connectivity over centimeters via capillary-driven corner or thin-film flow. Concentration gradients further promote molecular diffusion within these films.

Figure 1A (xz, yz views) shows uneven residual brine patches post-drainage, with more brine retained in smaller pores due to varying capillary pressures (Fig. 1, xz, yz). After drainage, the nearly immobile aqueous phase forms pools of different sizes. Unsaturated CO₂ injection drives evaporation of water from these patches into the gas stream. Zoomed t₁–t₃ stages (Fig. 1B–D) reveal euhedral to subhedral cubic halite crystals (>100 μm) alongside smaller, aggregating micro-crystals. These large crystals contradict assumptions that only dispersed, micron-sized crystals form in 3D porous media, in contrast to observations made in 2D microfluidic

systems (13, 15, 39–42). Our findings demonstrate that advection, supersaturation, and confinement can foster substantial crystal growth, challenging models predicting minimal flow obstruction by distributed solids, necessitating their reevaluation.

Pore-scale dynamics from t1–t3 reflect microscale diffusion and transport. CO₂ invasion displaces brine, forming evaporative fronts where water evaporates into the gas phase. Initially limited brine-gas interfaces slow evaporation, but supersaturated micro-environments drive halite crystallization via local concentration gradients and ion movement to growth sites. Increased brine-gas contact and ongoing evaporation sustain ion supply, promoting crystal growth, especially at supersaturated interfaces (Fig. 1). Wettability of the porous medium (beads, crystals) shapes salt distribution and morphology. Continuous evaporation, ion transport, nucleation and growth form new crystals atop or beside existing ones, creating secondary porous media (37, 43–45). Such porous media, with small pores exert strong capillary forces, imbibing brine, while hydrophilic substrates maintain liquid films as solute transport pathways, enabling crystallization even away from bulk brine.

Figures 1B–C (xy profiles i–iii) show increased precipitation in 1C over 1B, with t3 exhibiting greater brine imbibition than t2. Conversely, profiles iv–vi indicate dissolution events, reflecting a dynamic feedback loop of precipitation, dissolution, and capillary forces. Local brine patches alternate between dissolution and re-precipitation, driving morphological changes and capillary gradients. Ongoing concentration shifts create gradients, potentially triggering Marangoni or diffusive flows.

Across the three stages in Figure 1, crystalline structures expand and interconnect, forming salt networks that alter pore geometry, porosity and permeability. Local dissolution and re-precipitation occur (Fig. 1A–C, xy views iv–vi), likely due to fluctuating saturation, brine flow, or evaporation rates. This interplay reflects transient micro-environments, with concentrated brine near crystals driving both deposition and resorption. Brine movement in interconnected voids sustains a feedback loop of solute redistribution, dissolving salt in some areas while supersaturation elsewhere accelerate crystal growth and reactive surface area for further precipitation.

Figure 1E shows brine and salt interplay around a glass bead (cast), with segmented images revealing a continuous liquid film on the bead's surface topped by salt precipitates. Direct salt-bead contact highlights preferential nucleation at low-energy sites. The 3D salt structure exhibits internal voids and intercrystallite porosity from aggregating patches, sustaining dynamic equilibrium by enabling brine access.

A comparison between the t1 and t2-t3 stages indicates that in t1, the residual brine is primarily confined to specific sections of the porous medium. This confinement restricts the evaporation rate due to the limited contact area between the gas stream and the receding/evaporating aqueous phase. In the xy-sections (Fig. 1), it is evident that in addition to salt crystallization occurring in bulk aqueous phases (brine pools), a significant portion of halite crystallization takes place at the interfaces between the brine and gas percolation pathways. Regions experiencing high evaporation rates, such as the brine-gas interface, can induce localized supersaturation, promoting crystal growth even in the presence of liquid brine. Evaporation from brine films- that are held by surface tension around the crystals- can lead to the formation of highly concentrated pockets of aqueous phase. These pockets are particularly conducive to further crystal growth. Maintaining this dynamic equilibrium involves intricate balances between evaporation, solute transport, and crystallization kinetics. Continuous growth form a feedback loop that sustains the process, ensuring the coexistence of liquid brine and growing salt crystals.

Tomography images from t1 (Fig. 1A, xz, yz views) shows salt precipitation and creeping along the flow cell's inner walls in the z-direction. This reflects how cell geometry and surface properties direct the aqueous phase, sustaining halite precipitation around glass beads. The hydrophilic walls and confinement create supersaturated micro-environments via preferential evaporation, fostering salt growth sites and a continuous crystalline network extending over a centimeter in the z-direction.

An intriguing aspect of the observations from t1 to t3 (Fig. 1) is the coexistence of aqueous phase (brine) and precipitated solid phases (halite crystals). This dynamic equilibrium raises questions about the conditions that support continued salt crystal growth in the presence of a liquid phase, which one might intuitively expect only to dissolve the halite crystals rather than facilitate precipitation. The liquid phase must be supersaturated for the continued growth of halite crystals. The highly concentrated brine films around the crystals, retained by surface tension, act as reservoirs of concentrated ionic solutions, perpetuating the growth of existing crystals. Additionally, capillary effects maintain a delicate balance that prevents dissolution and supports ongoing precipitation.

Evaporation-precipitation dynamics and crystallization patterns

Figure 2 tracks the experiment from t_1 to t_5 , showing brine-salt coexistence evolving into extensive salt precipitation in a fully dried pore space. At t_1 , brine and salt coexist with initial growth; by t_5 , micro-CT reveals widespread salt filling the pores (Fig. 2A–B). In t_1 and t_3 , salt nucleates and grows in brine-saturated regions and at liquid-gas interfaces, driven by substrate wettability (Figs. 2A–B). As brine shrinks, halite forms at these interfaces, consuming residual liquid. Large crystals nucleate through solute self-assembly in the liquid phase, similar to the video snapshot presented in (13), eventually extending into the surrounding gas stream and protruding into the gas-liquid interface. These crystals form at moderate rates within the brine pools, steadily developing their crystalline structures.

Accelerated evaporation and brine consumption (15) form micron-sized halite aggregates at menisci in t_1 – t_3 , appearing as dense, varied salt patches at gas-liquid interfaces (Fig. 2C). With sufficient solute from nearby brine, these evolve into disordered, interconnected crystals by t_5 , creating a secondary porous medium (Fig. 2B–D). In t_4 – t_5 , forced evaporation depletes large brine pools, shifting from large crystal formation to micron-sized aggregates due to rapid brine loss and heightened evaporation. Disrupted brine film continuity in these stages further increases aqueous phase consumption.

In this water-wet system, polycrystalline aggregates form dendritic structures via continuous brine films (Fig. 2A&E), driven by diffusion-limited growth, capillary suction, and local solute gradients. This pattern increases evaporation and reactive surface areas, enhancing capillary action. At the shrinking brine interface (Fig. 2B, t_1 & t_3), increased curvature confines brine, lowering the energy barrier for halite nucleation and accelerating crystallization. Brine films on hydrophilic surfaces transport ions from adjacent patches (Figs. 1E & 2A), merging micron-sized crystals into complex structures that fill pore spaces. Capillary flow sustains solute supply, maintaining supersaturation for nucleation on secondary substrates, leading to interconnected crystal networks that alter morphology, capillarity, and hydrodynamics.

In the final stages (t_4 – t_5), crystallization evolves as long as brine persists, predominantly occurring on salt surfaces that facilitate residual brine migration from bead surfaces. Solutes are drawn toward precipitation sites via strong capillary-driven flow. The hydrophilic nature of salt crystals promotes ion retention on their surfaces, fostering more intricate aggregates than the initial micron-scale halite interconnections. This increasingly obstructs pore throats and flow pathways, significantly reducing permeability (Fig. 2A, t_5). Figure 2C (inset) emphasizes the importance of brine saturation in shaping salt aggregates. Residual brine within these structures sustains continued crystal growth, giving rise to a “wet salt” morphology at t_5 . Even at this stage, internal brine saturation persists, highlighting the role of capillarity and surface interactions in maintaining local supersaturation. With prolonged oven drying, this brine eventually evaporates, leaving behind a fully dried salt patch with only minor additional crystallization evident in the final tomogram.

Figures 2D–E display tomograms and segmented images of the dried pore space, illustrating how distinct precipitation patterns occupy the available pore volume. These visualizations capture the spatial distribution and morphological features of halite crystals formed via evaporation-driven precipitation. Key observations include:

- The topmost layers exhibit dense, umbrella-like crusts formed by progressive halite accumulation at the gas–brine interface, where evaporation is most intense. These crusts trap residual brine within the pore space, sustaining crystal growth while simultaneously inhibiting further evaporation, thereby prolonging the drying process.
- Within the aggregates, a porous network of sub-micron halite crystals is interspersed with voids and potentially brine-coated surfaces. These structures trap isolated brine pockets, reflecting a dynamic balance between crystallization and liquid retention.
- Distinct cubic halite crystals are observed beneath the crust, typically on the micron scale, indicating localized growth conditions.
- Halite nucleates at the brine–gas interface and grows outward into the gas phase, generating voids between the salt and bead surfaces. This results from halite expanding into the less viscous gas environment, leaving behind interstitial brine, which remains mobile and redistributes via capillary action.
- Continued brine supply fosters the growth of secondary salt aggregates. These structures form interconnected porous networks that influence fluid flow and ion transport, with microcrystals coalescing into spatially complex assemblies.

The formation of a thin liquid film initiates a dynamic cycle of crystal growth and aggregation. Initially, nascent crystals consume the local supersaturation within the film until saturation equilibrium is reached. At this point, concentration gradients and capillary forces drive additional water and solutes toward the crystallization front. Once supersaturation is reestablished, nucleation resumes on existing substrates. This repeated cycle of film replenishment and supersaturation fosters the development of porous salt aggregates (see Fig. 5, Discussion).

This process can be cyclic and discontinuous when crystal growth lags behind solute transport and a critical nucleation threshold exists. Under such conditions, solute delivery enables local saturation to rise until it exceeds the nucleation threshold, initiating new crystal formation. In this particular porous medium, capillary backflow and solute diffusion may outpace crystallization, promoting intermittent nucleation events. This has direct implications for evaporation dynamics: rapid evaporation accelerates solute accumulation, favoring nucleation over sustained crystal growth. Disentangling the relative influence of evaporation versus solute flux remains complex. While rapid evaporation is widely recognized as a key driver of salt aggregation (15, 46–48), cyclic processes involving repeated evaporation and re-dissolution suggest solute transport also significantly modulates crystallization and aggregate evolution.

The formation of dense surface crusts, complex internal crystal networks, and secondary porous structures underscores the intricacy of halite precipitation dynamics. To quantify the evolution of brine and salt accumulation, segmented phase volumes were plotted across time points t_1 – t_5 , alongside void fraction estimates (Fig. 2F). Glass beads comprise approximately $60\% \pm 2\%$ of the total volume, with the remainder distributed among brine, halite, and voids. Kernel density estimates (KDEs; see Materials and Methods) were included to represent the smoothed probability distributions of phase volumes, providing insight into both concentration and variability.

Between t_4 and t_5 , salt volume increases only marginally, stabilizing around 10%, while porosity remains near 30% in the final stage. The rising brine volume during intermediate stages reflects capillary-driven film flow that sustains halite growth. As brine is drawn toward the evaporation front, the segmented brine volume increases, supplying ions required for continued crystallization (Fig. 2F). The limited salt growth between t_4 and t_5 suggests depletion of accessible brine, with void space increasing as water saturation approaches zero.

Figure 2 illustrates crystallization patterns that significantly impact pore space characteristics, including the porosity-permeability relationship. Growth into the pore volume leads to obstruction of throats and connected pathways, resulting in banded aggregate formations (Fig. 2D). These crystallization patterns create localized blockages within the pore network, consistently hindering fluid flow. While this obstruction causes a moderate reduction in porosity, as demonstrated here, it can lead to a substantial decrease in permeability (12, 49). This raises a critical question for the following section: can porous or semi-porous aggregates evolve into non-porous forms, or develop sub-resolution intercrystalline porosity through densification or microstructural reorganization?

Texture and internal growth structure of halite precipitation

High-resolution scanning electron microscopy (Figs. 3A–B) reveals two distinct halite surface textures within the same sample. Figure 3A shows a smooth, dense, non-porous or nano-porous texture with minimal visible porosity, while Figure 3B displays a micro-porous texture of interconnected crystals and channels. The non-porous texture (Fig. 3A) reflects rapid crystallization under high supersaturation and evaporation rates, forming compact surfaces with few voids. Conversely, the micro-porous texture (Fig. 3B) suggests slower growth in a heterogeneous environment, driven by variable supersaturation, capillary forces, and dynamic evaporation. Interconnected pores and channels indicate brine films sustain solute transport, supporting aggregate expansion. These textures highlight differing geochemical and thermodynamic conditions influencing halite crystallization.

To investigate porous and semi-porous halite aggregates seen in electron microscopy, we analyzed multiple halite bodies to trace the transition from porous to non-porous structures or sub-resolution intercrystalline porosity during crystallization, shaping distinct surface patterns. Using X-ray tomography (Figs. 3C, 3E), we reconstructed 3D internal structures of the top umbrella-like crust and middle halite body, targeting an apparently non-porous crust section and potentially porous interior. The extracted crusts, segmented for salt and porosity, reveal intricate 3D patterns and connectivity, with ~40% internal porosity in a region once thought

non-porous. Pore network modeling using OpenPNM (50) via connected components multi-ROI analysis (Fig. 3D) quantifies this: pore diameters range from 20–200 μm (average 70 μm , 95th percentile 100 μm), and connectivity averages 5 (range 1–26). Over 95% of pores have surface areas $<0.12\text{ mm}^2$ (average 0.04 mm^2). These metrics support capillary force calculations for hydrophilic halite structures and provide realistic reactive surface data for modeling CO_2 -induced halite growth (12, 45, 49).

Unlike the compact crust, the internal halite body shows a highly porous architecture ($>62\%$ porosity) with diverse crystal shapes and sizes (Figs. 3E–F). A cylindrical section, segmented into halite and porosity phases, reveals internal voids and layered, fishbone-like patterns in 2D profiles. Composed of small pillars and lateral surfaces, these layers form euhedral to subhedral cubic crystals, expanding into pore spaces via coalescence with base and crust layers. The porosity exhibits strong horizontal and vertical connectivity.

Differences in porosity and texture between the two structures reflect nucleation and growth rate interplay. High supersaturation drives rapid precipitation, forming dense crystals with few voids, while lower supersaturation enables brine redistribution, creating micropore networks. This aligns with Desarnaud et al. (44), noting closed crusts at low relative humidity (RH) due to fast evaporation, versus open crusts at higher RH, termed patchy (open) and crusty (closed) efflorescence in the literature.

Pore volume vs. inscribed diameter analysis of the salt body (Figs. 3C–D) is shown in Figure 3G with frequency plots. Most pores ($<70\text{ }\mu\text{m}$ diameter, $<0.003\text{ mm}^2$ volume) cluster in the bottom left, with larger pores tied to surface voids (Fig. 3G). Internal porosity analysis across multiple ROIs, normalized to the highest volume (Fig. 3H), shows increasing porosity with scale ($\sim 35\% \pm 15\%$), with broader scatter in larger volumes (>0.75 normalized) and narrower scatter in smaller ones (<0.2). A best-fit trend and kernel density estimate highlight scale-dependent heterogeneity, with larger volumes exhibiting greater structural variability and porosity, while smaller volumes appear more uniform.

Spectral tomography analysis of salt precipitation

Spectral X-ray micro-computed tomography (Sp-CT) analyzes salt precipitation, focusing on compositional and density variations via the linear attenuation coefficient (μ), which quantifies X-ray beam attenuation across an energy spectrum. Higher μ reflects stronger attenuation, driven by composition (Z) and density (ρ). Density effects are energy-independent, while Z effects dominate at low energies (21–31 keV) versus high energies (51–61 keV), enabling differentiation of halite's dense and low-density aggregates.

Figure 4A shows multi-energy histograms from these ranges, with average μ profiles per pixel in Figure 4B. A μ_{low} vs. μ_{high} crossplot (Fig. 4C) uses color to indicate pixel fractions, clustering into fluid phase, glass flow cell, glass beads (regions 1–3), and halite aggregates (region 4), as segmented in Figure 4D. Halite trends reveal density variations: low μ values mark low-density regions, while high μ values indicate dense precipitates. Segmented images (Figs. 4E–F) show halite growing on glass beads and into pore spaces, with density tied to internal porosity and inter-crystalline spaces.

Halite aggregates feature dense cores encased by lower-density growth at top and bottom, reflecting initial macro-crystal formation followed by micro-crystallites, consistent with the salt coffee-stain effect (51, 52). Umbrella-like structures, however, create internal pore volumes with low-density salts (Fig. 4F). Growth tips extending into pores or merging with adjacent aggregates also exhibit low-density precipitation.

Discussion and Conclusions

Mechanisms regulating halite's self-enhancing growth

Halite's self-enhancing growth during CO_2 injection in saline aquifers arises from thermodynamic, hydrodynamic, and structural interactions. Thermodynamically, nucleation and crystal growth depend on local supersaturation, driven by ionic concentration, temperature, and evaporation rates, with classical nucleation theory linking supersaturation to nucleation kinetics and reactive surface area (53). Capillary action sustains supersaturation by supplying brine, promoting rapid crystal aggregation and porous microstructures (Figs. 1–3).

Two mechanisms accelerate growth. First, evaporation shifts the gas-liquid interface from larger to finer pores, expanding the surface area for brine evaporation and salt formation. Second, hydrophilic, hygroscopic halite crystals, nucleating on existing precipitates as secondary substrates (37, 45), amplify reactive surface area and create a feedback loop. These crystals attract brine films, enhance evaporation and serving as low-

energy nucleation sites (54), forming micron-sized aggregates ($\sim 0.04 \text{ mm}^2$ mean surface area, Fig. 3D) before complete drying.

The resulting porous structures (Fig. 3) intensify capillary suction, drawing brine to the evaporation front and increasing local supersaturation at the shrinking aqueous interface, lowering nucleation energy barriers (55, 56). Thin brine films on hydrophilic surfaces deliver ions, enabling complex, pore-filling aggregates. However, salt crusts or umbrella-like structures (Figs. 2–3) can cover brine surfaces, reducing gas-liquid exposure and slowing evaporation as thermal insulators. While trapped brine evaporates more slowly, precipitation persists through fissures, balancing growth acceleration and inhibition.

Five interconnected drivers nurture halite's self-enhancing growth:

A. Nucleation at gas-liquid interface

Nucleation at the gas-liquid interface shapes halite crystallization, driven by rapid evaporation and supersaturation. Reduced interfacial tension and elevated solute concentrations (vs. solid interfaces) promote ion aggregation into stable nuclei (37, 55, 56). This self-perpetuating cycle (evaporation fueling nucleation and nuclei attracting ions) yields dense, finely distributed crystals, setting the stage for expansive precipitation.

B. Porous salt structures

Halite's porous networks ($\sim 40 \pm 15\%$ porosity, Fig. 3) emerge from crystal interconnections near secondary substrates, with pores ($< 100 \mu\text{m}$ to nm) generating strong capillary pressures. Enhanced by meniscus curvature and evaporation gradients (57, 58), these structures sustain brine influx, forming a feedback loop that transforms aggregates into complex scaffolds.

C. Concentration gradient near evaporation front

Evaporation creates steep concentration gradients (24), peaking at the drying interface (e.g., near-wellbore) and declining inward (3, 12). Governed by Fick's laws, diffusive ion flux sustains supersaturation (47), with higher evaporation rates (47) and Marangoni effects (59–61) accelerating nucleation and growth.

D. Substrate wettability

Hydrophilic surfaces stabilize thin brine films via low contact angles, ensuring solute transport to evaporation fronts (15, 62, 63). Halite's hydrophilicity and hygroscopicity retain moisture, maintaining local supersaturation (64, 65), fostering continuous nucleation and growth. The matrix-driven film stability and salt-driven moisture retention is particularly important in dynamic environments, such as near-wellbore regions prone to localized drying.

E. Capillary-induced brine film flow

Capillary-induced brine film flow drives CO_2 -induced salt precipitation, transporting solutes through thin liquid layers across porous media (66, 67). Film flow is governed by surface tension, adhesion, and capillary suction (67). It operates from micrometers within pores to centimeters across networks (68), linking brine reservoirs to evaporation fronts near injection wells. Efficacy depends on pore connectivity, hydraulic conductivity, and drying site distribution, with halite's hygroscopicity enhancing capillary pull into growing salt structures.

Advection delivers solutes to the evaporation front, outpacing diffusion (33), with the Péclet number (Pe) governing their competition (69). When advection dominates ($\text{Pe} \gg 1$), solute accumulation triggers nucleation and precipitation. Halite crystals form porous structures (12, 49), increasing connectivity and capillary suction via smaller pores. This feedback loop, linked to factors A–D, sustains growth by supplying supersaturated brine to nucleation sites. The interplay between crystallization and capillary forces ties salt growth rates to evaporation flux, dynamically reshaping pore geometry and fluid dynamics.

Figure 5 illustrates the key physical processes driving halite's self-enhancing growth during CO_2 injection in saline aquifers: (a) two-phase viscous displacement, (b) capillary-driven backflow, (c) evaporation and salt diffusion, (d) self-enhancing growth, and (e) concentration gradients from ion consumption. Injected CO_2 displaces brine via viscous forces, trapping residual brine, while undersaturated CO_2 triggers evaporation, concentrating salts at the drying interface (Fig. 5a). Hydrophilic substrates sustain brine films, enabling capillary backflow to replenish solutes against CO_2 advance (Fig. 5b), enhanced by wettability and film flow. Evaporation creates gradients, driving diffusive ion transport (Fig. 5c), though low injection rates may homogenize distribution. Supersaturation brings about nucleation and precipitation, with porous salt structures enhancing

capillary suction and solute supply, fostering growth that alters porosity and permeability (Fig. 5d). Ion consumption steepens gradients, promoting diffusion to active sites (Fig. 5e).

Future directions for characterization of salt self-enhancing growth

Saline aquifers during CO₂ storage exhibit dynamic fluid movement governed by capillary, viscous, and gravity forces, with capillary action driving wicking, which is the spontaneous liquid transport through porous media via capillary suction at liquid-gas interfaces (70–72) to sustain solute replenishment at the evaporation front (Fig. 5). These force interactions govern fluid movement, solute transport, and salt deposit evolution, yet current reactive transport models lack a unified approach to quantify them, limiting understanding of self-enhancing growth. We propose integrating following key dimensionless numbers, Capillary (viscous-to-capillary forces), Bond (gravity vs. surface tension), Péclet (advection-diffusion balance), Damköhler (precipitation vs. transport rates), and Weber (inertial-to-surface tension forces) to clarify force dominance and reconcile literature gaps. These metrics address fluid displacement, buoyancy-driven brine migration, solute distribution, reaction-transport regimes, and brine film stability, respectively. Gravity-driven migration and re-imbibition sustain near-wellbore solute sources, complementing capillary effects, though further study is needed. This framework enhances mechanistic insights into multi-scale dynamics, improving reactive transport model accuracy and informing CO₂ storage strategies to preserve permeability and injectivity.

Materials and Methods

Experimental design

This study investigated pore-scale halite precipitation patterns and growth dynamics within a porous medium of glass beads. A custom cylindrical glass flow cell (7 mm OD, 100 mm height) packed with 2 mm glass beads was used to examine salt growth driven by brine film movement under viscous, gravitational, and capillary forces. The porous network was saturated with 5 M NaCl solution, followed by CO₂ injection at 1 MPa to achieve residual brine saturation, and then subjected to evaporation and precipitation under a 5 ml/min gas stream. Salt crystals formed in the top 25 mm of the column were imaged (t1). Subsequent stages involved spontaneous evaporation under ambient conditions (t2, t3) and accelerated evaporation at 60°C (t4, t5), with imaging conducted after each stage. Post-experiment halite aggregates on glass beads were also scanned for detailed analysis. A detailed description is provided in the Supporting Information (SI).

Time-lapse X-ray tomography of evolution dynamics (micro-CT)

To study the evolution dynamics of halite precipitation, time-lapse X-ray micro-CT imaging was conducted at multiple stages. Initial imaging at time t1 served as the reference, followed by monitoring of evaporation and precipitation under ambient conditions at t2 and t3, and after induced evaporation at elevated temperatures at t4 and t5. This enabled tracking of the 3D structural growth of salt aggregates and brine consumption until complete drying. Imaging was performed using a Tescan UniTOM XL Spectral at 60 kV and 14 W, with full-sample scans (2142 frames, 85 ms exposure, 5 μm/voxel) and zoomed scans (2700 frames, 200 ms exposure, 2.5 μm/voxel). Data were reconstructed using Panthera (v 1.4.3.16), focusing on the active evaporation-precipitation region at the column top for consistency across all time points. See SI for details.

Spectral X-ray micro-computed tomography (Sp-CT)

Spectral X-ray imaging was employed to enhance contrast over conventional micro-CT by detecting the energy spectrum of transmitted X-rays, providing energy-dependent attenuation coefficients that reveal compositional and density details of salt structures. Imaging was conducted using a Tescan UniTOM XL Spectral at the DMEX Center (Pau, France) with a CdTe-detector (307 mm width, 764 x 1 pixels, 140 keV bins). Over 20 minutes, 800 projection images were collected during a 360° rotation and reconstructed into spectral slices with a 9.5 μm voxel size using Tescan Spectral Suite (v. 2.1.0.108). Details are given in the SI.

Electron microscopy

Scanning electron microscopy (SEM) with backscattered electron (BSE) and secondary electron (SE) imaging was used to examine post-experiment growth structures. SE imaging provided detailed surface structure

information, while BSE imaging offered insights into deeper regions and sensitivity to atomic numbers. A variable-pressure Hitachi SU5000 FE-SEM with a Dual Bruker XFlash system and high-resolution electron backscatter diffraction was employed. Specimens were carbon-coated using a Cressington 208C coater to enhance image quality, improve chemical analysis precision, and prevent surface charging and thermal damage. Full description in SI.

Image post-processing and segmentation

Tomography images were processed using Dragonfly (v2024.1) and an in-house Python pipeline. After noise reduction via filtering, an AI-assisted deep learning (DL) approach with a U-Net convolutional neural network (depth 5, 64 initial filters) was implemented for image segmentation to distinguish material phases with overlapping signatures. The model was trained with a $64 \times 64 \times 1$ patch size, 0.25 stride ratio, 256 batch size, and 100 epochs, using Categorical Crossentropy loss and Adadelta optimization, with data augmentation (flipping, rotating up to 180° , zooming 0.9–1.1, shearing 2.0°) to enhance robustness. This enabled precise differentiation of flow cell components (glass beads, salt crystals, brine, air) and analysis of halite crystallization dynamics. Kernel Density Estimation (KDE) was used in Figures 2–3 to visualize data variability across temporal stages, with distribution clouds, $\pm 5\%$ confidence intervals, and optimized bandwidth selection to balance smoothness and fidelity, revealing trends without distortion. Details are in the SI.

Acknowledgments

Funding: This work was supported by the “Understanding Coupled Mineral Dissolution and Precipitation in Reactive Subsurface Environments” project, funded by the Norwegian Centennial Chair (NOCC) as a transatlantic collaboration between the University of Oslo (Norway) and the University of Minnesota (USA). The authors also acknowledge support from the Excite Network for granting transnational access to the DMEX facility (UPPA, France), funded by the European Union’s Horizon 2020 research and innovation programme under grant agreement No. 101005611, and Horizon Europe under grant agreement No. 101131765. H. Derluyn acknowledges the support from the European Research Council (ERC) under the European Union’s Horizon 2020 research and innovation programme (grant agreement No 850853)”.

Competing interests: Authors declare that they have no competing interests.

Data availability: All tomography data used in the analyses will be made available for the purpose of extending and reproducing the analyses, subject to a Material Transfer Agreement (MTA). The data will be deposited in the DataverseNO public database and will be accessible with a designated DOI upon publication.

References

1. E. C. D.-G. for C. Action, *Going climate-neutral by 2050 – A strategic long-term vision for a prosperous, modern, competitive and climate-neutral EU economy* (Publications Office, 2019).
2. “Europe’s 2040 climate target and path to climate neutrality by 2050 building a sustainable, just and prosperous society (COM(2024) 63 final)” (2024).
3. R. Miri, H. Hellevang, Salt precipitation during CO₂ storage—A review. *INT J GREENH GAS CON* **51**, 136–147 (2016).
4. X. Sun, *et al.*, A review of experimental investigations on salt precipitation during CO₂ geological storage. *Geoenergy Sci. Eng.* **244**, 213451 (2025).
5. G. Cui, Z. Hu, F. Ning, S. Jiang, R. Wang, A review of salt precipitation during CO₂ injection into saline aquifers and its potential impact on carbon sequestration projects in China. *Fuel* **334**, 126615 (2023).
6. S. Grude, M. Landrø, J. Dvorkin, Pressure effects caused by CO₂ injection in the Tubåen Fm., the Snøhvit field. *INT J GREENH GAS CON* **27**, 178–187 (2014).
7. S. Talman, A. R. Shokri, R. Chalaturnyk, E. Nickel, “Salt Precipitation at an Active CO₂ Injection Site” in *Gas Injection into Geological Formations and Related Topics*, (2020), pp. 183–199.
8. G. Baumann, J. Henniges, M. De Lucia, Monitoring of saturation changes and salt precipitation during CO₂ injection using pulsed neutron-gamma logging at the Ketzin pilot site. *INT J GREENH GAS CON* **28**, 134–146 (2014).
9. J. Mahadevan, M. M. Sharma, Y. C. Yortsos, Capillary Wicking in Gas Wells. *SPE J.* **12**, 429–437 (2007).
10. M. Nooraiepour, *et al.*, Potential for 50% Mechanical Strength Decline in Sandstone Reservoirs Due to Salt Precipitation and CO₂–Brine Interactions During Carbon Sequestration. *Rock Mech. Rock Eng.* (2024). <https://doi.org/10.1007/s00603-024-04223-8>.
11. H. Ott, J. Snippe, K. de Kloe, Salt precipitation due to supercritical gas injection: II. Capillary transport in multi porosity rocks. *Int. J. Greenh. Gas Control* **105**, 103233 (2021).
12. M. Masoudi, H. Fazeli, R. Miri, H. Hellevang, Pore scale modeling and evaluation of clogging behavior of salt crystal aggregates in CO₂-rich phase during carbon storage. *Int. J. Greenh. Gas Control* **111**, 103475 (2021).
13. M. Nooraiepour, H. Fazeli, R. Miri, H. Hellevang, Effect of CO₂ Phase States and Flow Rate on Salt Precipitation in Shale Caprocks - A Microfluidic Study. *Environ. Sci. Technol.* **52**, 6050–6060 (2018).
14. M. Khosravi, E. H. Stenby, W. Yan, Simulation analysis of salt precipitation in large-scale CO₂ storage using periodic injection via a horizontal well. *Int. J. Greenh. Gas Control* **138**, 104263 (2024).
15. K. M. Dąbrowski, *et al.*, Surface wettability governs brine evaporation and salt precipitation during carbon sequestration in saline aquifers: Microfluidic insights. *Sci. Total Environ.* **958**, 178110 (2025).
16. V. Darkwah-Owusu, M. A. M. Yusof, Y. A. Sokama-Neuyam, J. N. Turkson, I. Fjelde, A comprehensive review of remediation strategies for mitigating salt precipitation and enhancing CO₂ injectivity during CO₂ injection into saline aquifers. *Sci. Total Environ.* **950**, 175232 (2024).
17. G. J. G., B. Usman, The Endurance CO₂ storage site, Blocks 42/25 and 43/21, UK North Sea. *Geol. Soc. London, Mem.* **52**, 163–171 (2020).
18. W. D. Peck, *et al.*, CO₂ Storage Resource Potential of the Cambro-ordovician Saline System in the western Interior of North America. *Energy Procedia* **37**, 5230–5239 (2013).
19. G. Shi, J. Wang, I. D. Gates, Combined geothermal and CO₂ sequestration in the Basal Cambrian Sandstone Unit (BCSU) in Alberta, Canada. *J. CO₂ Util.* **80**, 102685 (2024).
20. H. Würdemann, *et al.*, CO₂SINK—From site characterisation and risk assessment to monitoring and verification: One year of operational experience with the field laboratory for CO₂ storage at Ketzin, Germany. *Int. J. Greenh. Gas Control* **4**, 938–951 (2010).
21. E. Mehnert, P. H. Weberling, Groundwater Salinity within the Mt. Simon Sandstone in Illinois and Indiana. *Circ. no. 582* (2014).
22. J. Freiburg, *et al.*, *Subtask 7.2 Wabash CarbonSAFE Geology of the Mt. Simon Sandstone Storage Complex (1)* (2022).
23. N. H. Schovsbo, *et al.*, Types of formation water and produced water in Danish oil- and gasfields: implications for enhanced oil recovery by injection of ‘smart’ water. *GEUS Bull.* **35**, 43–46 (2016).
24. N. Shokri, A. Hassani, M. Sahimi, Multi-Scale Soil Salinization Dynamics From Global to Pore Scale: A Review. *Rev. Geophys.* **62**, e2023RG000804 (2024).
25. A. Hassani, A. Azapagic, N. Shokri, Global predictions of primary soil salinization under changing climate in the 21st century. *Nat. Commun.* **12**, 6663 (2021).
26. F. M. Allai, Z. R. A. A. Azad, N. A. Mir, K. Gul, Recent advances in non-thermal processing technologies for enhancing shelf life and improving food safety. *Appl. Food Res.* **3**, 100258 (2023).
27. R. K. Bund, R. W. Hartel, “7 - Crystallization in foods and food quality deterioration” in *Woodhead Publishing Series in Food Science, Technology and Nutrition*, L. H. Skibsted, J. Risbo, M. L. B. T.-C. D. and P. I. of F. and B. Andersen, Eds. (Woodhead Publishing, 2010), pp. 186–215.
28. S. J. C. Granneman, B. Lubelli, R. P. J. van Hees, Mitigating salt damage in building materials by the use of crystallization modifiers - a review and outlook. *J. Cult. Herit.* **40**, 183–194 (2019).

29. F. Caruso, T. Wangler, R. J. Flatt, Easy Illustration of Salt Damage in Stone. *J. Chem. Educ.* **95**, 1615–1620 (2018).
30. J. Desarnaud, F. Bertrand, N. Shahidzadeh-Bonn, Impact of the Kinetics of Salt Crystallization on Stone Damage During Rewetting/Drying and Humidity Cycling. *J. Appl. Mech.* **80** (2013).
31. R. J. Flatt, F. Caruso, A. M. A. Sanchez, G. W. Scherer, Chemo-mechanics of salt damage in stone. *Nat. Commun.* **5** (2014).
32. R. Flatt, *et al.*, Predicting salt damage in practice: A theoretical insight into laboratory tests. *RILEM Tech. Lett.* **2**, 108–118 (2017).
33. S. M. S. Shokri-Kuehni, M. Norouzi Rad, C. Webb, N. Shokri, Impact of type of salt and ambient conditions on saline water evaporation from porous media. *Adv. Water Resour.* **105**, 154–161 (2017).
34. H. Derluyn, *et al.*, Characterizing saline uptake and salt distributions in porous limestone with neutron radiography and X-ray micro-tomography. *J. Build. Phys.* **36**, 353–374 (2013).
35. H. Derluyn, *et al.*, Saline Water Evaporation and Crystallization-Induced Deformations in Building Stone: Insights from High-Resolution Neutron Radiography. *Transp. Porous Media* **128**, 895–913 (2019).
36. G. W. W. Scherer, Stress from crystallization of salt. *Cem. Concr. Res.* **34**, 1613–1624 (2004).
37. M. Nooraiepour, M. Masoudi, N. Shokri, H. Hellevang, Probabilistic Nucleation and Crystal Growth in Porous Medium: New Insights from Calcium Carbonate Precipitation on Primary and Secondary Substrates. *ACS Omega* **6**, 28072–28083 (2021).
38. M. Nooraiepour, M. Masoudi, N. Shorki, H. Hellevang, Precipitation-induced Geometry Evolution in Porous Media: Numerical and Experimental Insights based on New Model on Probabilistic Nucleation and Mineral Growth. *SSRN Electron. J. Proc. 16th Greenh. Gas Control Technol. Conf.* (2022). <https://doi.org/10.2139/ssrn.4272555>.
39. J. Desarnaud, H. Derluyn, J. Carmeliet, D. Bonn, N. Shahidzadeh, Hopper Growth of Salt Crystals. *J. Phys. Chem. Lett.* **9**, 2961–2966 (2018).
40. A. Naillon, P. Duru, M. Marcoux, M. Prat, Evaporation with sodium chloride crystallization in a capillary tube. *J. Cryst. Growth* **422**, 52–61 (2015).
41. R. Miri, R. van Noort, P. Aagaard, H. Hellevang, New insights on the physics of salt precipitation during injection of CO₂ into saline aquifers. *INT J GREENH GAS CON* **43**, 10–21 (2015).
42. M. Nooraiepour, H. Fazeli, R. Miri, H. Hellevang, Salt Precipitation during Injection of CO₂ into Saline Aquifers: Lab-on-Chip Experiments on Glass and Geomaterial Microfluidic Specimens. *SSRN Electron. J. Proc. 14th Greenh. Gas Control Technol. Conf.* (2018). <https://doi.org/10.2139/ssrn.3365553>.
43. M. Masoudi, M. Nooraiepour, H. Hellevang, The Effect of Preferential Nucleation Sites on the Distribution of Secondary Mineral Precipitates in *83rd EAGE Annual Conference & Exhibition*, (European Association of Geoscientists & Engineers, 2022), pp. 1–5.
44. J. Desarnaud, *et al.*, Drying of salt contaminated porous media: Effect of primary and secondary nucleation. *J. Appl. Phys.* **118**, 114901 (2015).
45. M. Nooraiepour, M. Masoudi, H. Hellevang, Probabilistic nucleation governs time, amount, and location of mineral precipitation and geometry evolution in the porous medium. *Sci. Rep.* **11** (2021).
46. E. Lauga, M. P. Brenner, Evaporation-driven assembly of colloidal particles. *Phys. Rev. Lett.* **93**, 238301 (2004).
47. K. Roger, E. Sparr, H. Wennerström, Evaporation, diffusion and self-assembly at drying interfaces. *Phys. Chem. Chem. Phys.* **20**, 10430–10438 (2018).
48. M. Rezaei, R. R. Netz, Water evaporation from solute-containing aerosol droplets: Effects of internal concentration and diffusivity profiles and onset of crust formation. *Phys. Fluids* **33** (2021).
49. M. Masoudi, M. Nooraiepour, H. Deng, H. Hellevang, Mineral precipitation and geometry alteration in porous structures: How to upscale variations in permeability-porosity relationship? *Energy & Fuels* (2024). <https://doi.org/DOI: 10.1021/acs.energyfuels.4c01432>.
50. J. Gostick, *et al.*, OpenPNM: A Pore Network Modeling Package. *Comput. Sci. Eng.* **18**, 60–74 (2016).
51. N. Shahidzadeh, M. F. L. Schut, J. Desarnaud, M. Prat, D. Bonn, Salt stains from evaporating droplets. *Sci. Rep.* **5**, 10335 (2015).
52. N. Shahidzadeh-Bonn, S. Rafai, D. Bonn, G. Wegdam, Salt Crystallization during Evaporation: Impact of Interfacial Properties. *Langmuir* **24**, 8599–8605 (2008).
53. S. Auer, D. Frenkel, Suppression of crystal nucleation in polydisperse colloids due to increase of the surface free energy. *Nature* **413**, 711–713 (2001).
54. T. Nishinaga, *Handbook of Crystal Growth: Bulk Crystal Growth: Second Edition* (2014).
55. N. E. R. Zimmermann, B. Vorselaars, D. Quigley, B. Peters, Nucleation of NaCl from Aqueous Solution: Critical Sizes, Ion-Attachment Kinetics, and Rates. *J. Am. Chem. Soc.* **137**, 13352–13361 (2015).
56. M. W. Anderson, *et al.*, Understanding crystal nucleation mechanisms: where do we stand? General discussion. *Faraday Discuss.* **235**, 219–272 (2022).
57. S. M. Hassanizadeh, M. A. Celia, H. K. Dahle, Dynamic Effect in the Capillary Pressure–Saturation Relationship and its Impacts on Unsaturated Flow. *Vadose Zo. J.* **1**, 38–57 (2002).
58. Y. Chen, *et al.*, A Comprehensive Review of Factors Affecting Dynamic Capillary Effect in Two-Phase Flow. *Transp. Porous Media* **144**, 33–54 (2022).

59. M. Masoudi, M. Khosravi, B. Rostami, P. Abolhosseini, Effect of Bénard-Marangoni flow on the bypassed oil recovery: Micromodel study. *J. Pet. Sci. Eng.* **178**, 1067–1078 (2019).
60. P. Abolhosseini, M. Khosravi, B. Rostami, M. Masoudi, Influence of thermal Marangoni convection on the recovery of bypassed oil during immiscible injection. *J. Pet. Sci. Eng.* **164**, 196–205 (2018).
61. A. D. Nikolov, *et al.*, Superspreading driven by Marangoni flow. *Adv. Colloid Interface Sci.* **96**, 325–338 (2002).
62. A. Rufai, J. Crawshaw, Effect of wettability changes on evaporation rate and the permeability impairment due to salt deposition. *ACS Earth Sp. Chem.* **2**, 320–329 (2018).
63. N. Shahidzadeh-Bonn, *et al.*, Effect of wetting on the dynamics of drainage in porous media. *Transp. porous media* **56**, 209–224 (2004).
64. D. Benavente, M. A. G. del Cura, J. García-Guinea, S. Sánchez-Moral, S. Ordóñez, Role of pore structure in salt crystallisation in unsaturated porous stone. *J. Cryst. Growth* **260**, 532–544 (2004).
65. P. Zieger, *et al.*, Revising the hygroscopicity of inorganic sea salt particles. *Nat. Commun.* **8**, 15883 (2017).
66. M. Moura, E. G. Flekkøy, K. J. Måløy, G. Schäfer, R. Toussaint, Connectivity enhancement due to film flow in porous media. *Phys. Rev. Fluids* **4**, 94102 (2019).
67. M. Prat, On the influence of pore shape, contact angle and film flows on drying of capillary porous media. *Int. J. Heat Mass Transf.* **50**, 1455–1468 (2007).
68. P. Lehmann, S. Assouline, D. Or, Characteristic lengths affecting evaporative drying of porous media. *Phys. Rev. E* **77**, 56309 (2008).
69. L. Guglielmini, A. Gontcharov, A. J. Aldykiewicz, H. A. Stone, Drying of salt solutions in porous materials: Intermediate-time dynamics and efflorescence. *Phys. Fluids* **20** (2008).
70. S. Beyhaghi, S. Geoffroy, M. Prat, K. M. Pillai, Wicking and evaporation of liquids in porous wicks: A simple analytical approach to optimization of wick design. *AIChE J.* **60**, 1930–1940 (2014).
71. Y. T. Puyate, C. J. Lawrence, Steady state solutions for chloride distribution due to wick action in concrete. *Chem. Eng. Sci.* **55**, 3329–3334 (2000).
72. A. S. Goudie, Laboratory simulation of ‘the wick effect’ in salt weathering of rock. *Earth Surf. Process. Landforms* **11**, 275–285 (1986).

Figures

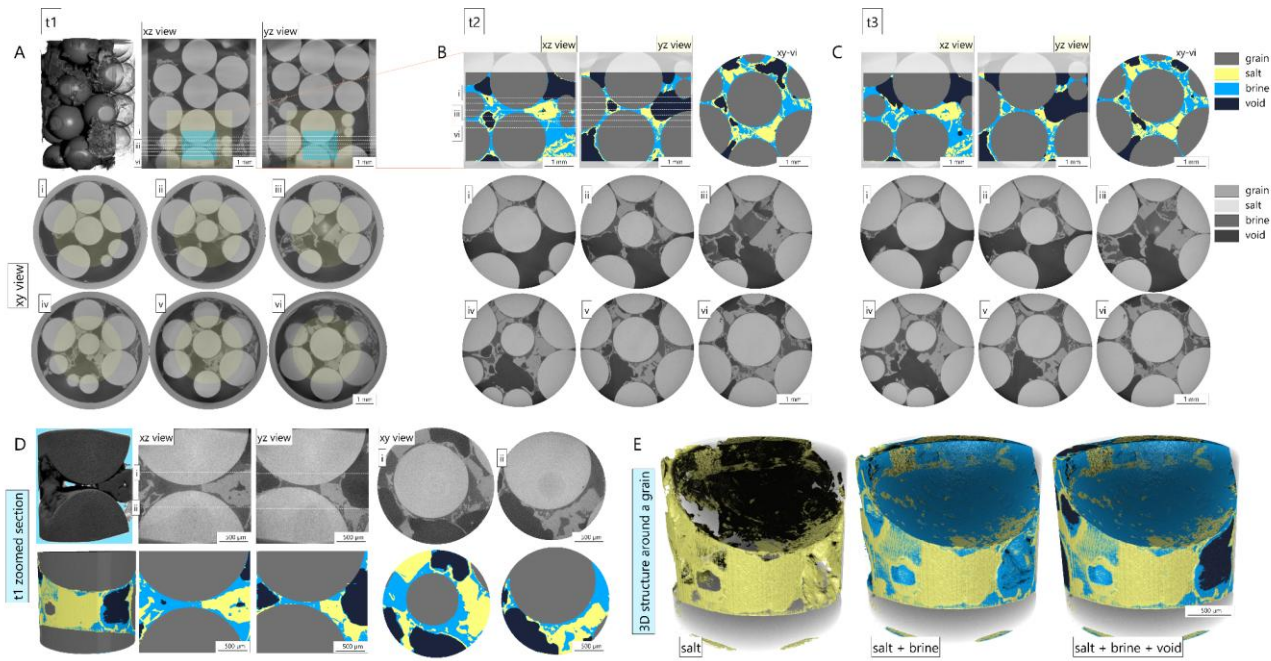


Figure 1. Brine-salt coexistence and crystallization-aggregation behavior. A-C. X-ray images and segmented counterparts during the first three temporal stages after establishing residual brine saturation and salt precipitation within the porous medium. The xz and yz cross-sections provide a vertical overview and six xy profiles present a horizontal section of brine and salt distribution. White dotted lines on the vertical cross sections (xz and yz views) indicate the locations displayed in the xy horizontal cross sections. D. The high-resolution zoomed-in section from t_1 presents detailed three-dimensional phase distributions of the aqueous and solid phases around a glass bead. E. Detailed coexistence of brine and salt around a glass bead (shown as cast), showing liquid phase spreading around beads while salt precipitates atop, forming porous patches.

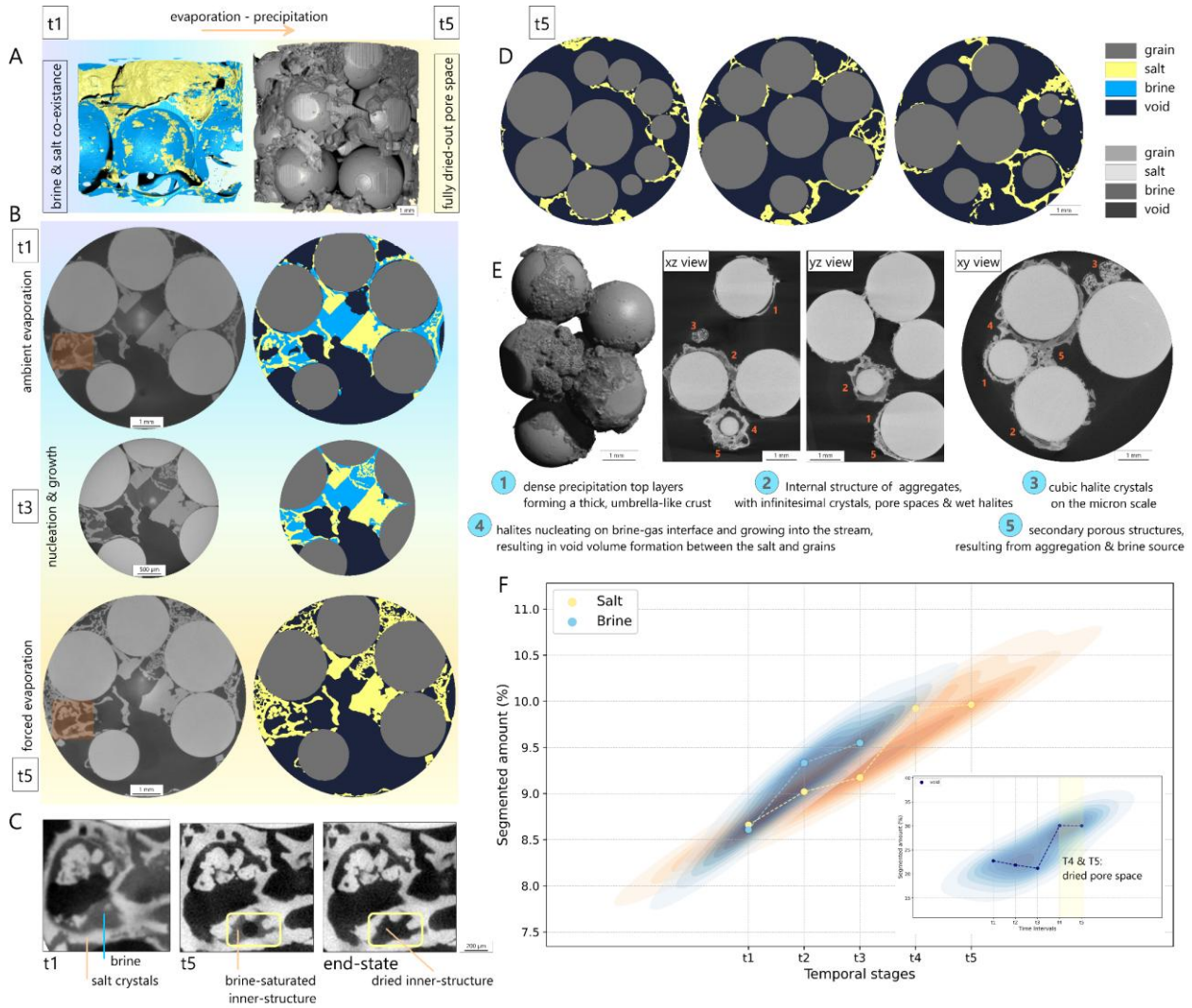


Figure 2. Evaporation-precipitation dynamics and crystallization patterns. A-B. Temporal timeline from t1 to t5 showing evolution from initial brine-salt coexistence to extensive salt precipitation in fully dried-out pore space, where X-ray tomograms and segmented images captured growth processes until experiments concluded. C. Zoomed-in section highlighting brine retention within salt structures during initial stages, supporting further growth under drying conditions. D. Segmented images of dried pore space at t5 from part B, illustrating various precipitation patterns and spatial distribution of halite crystals within the porous medium. E. 3D visualization and cross-sections showing internal complexity and porous structure of growing salt networks. F. Quantitative plot of segmented volumes of brine and halite over time, in addition to the void volume changes during intermediate halite precipitation stages.

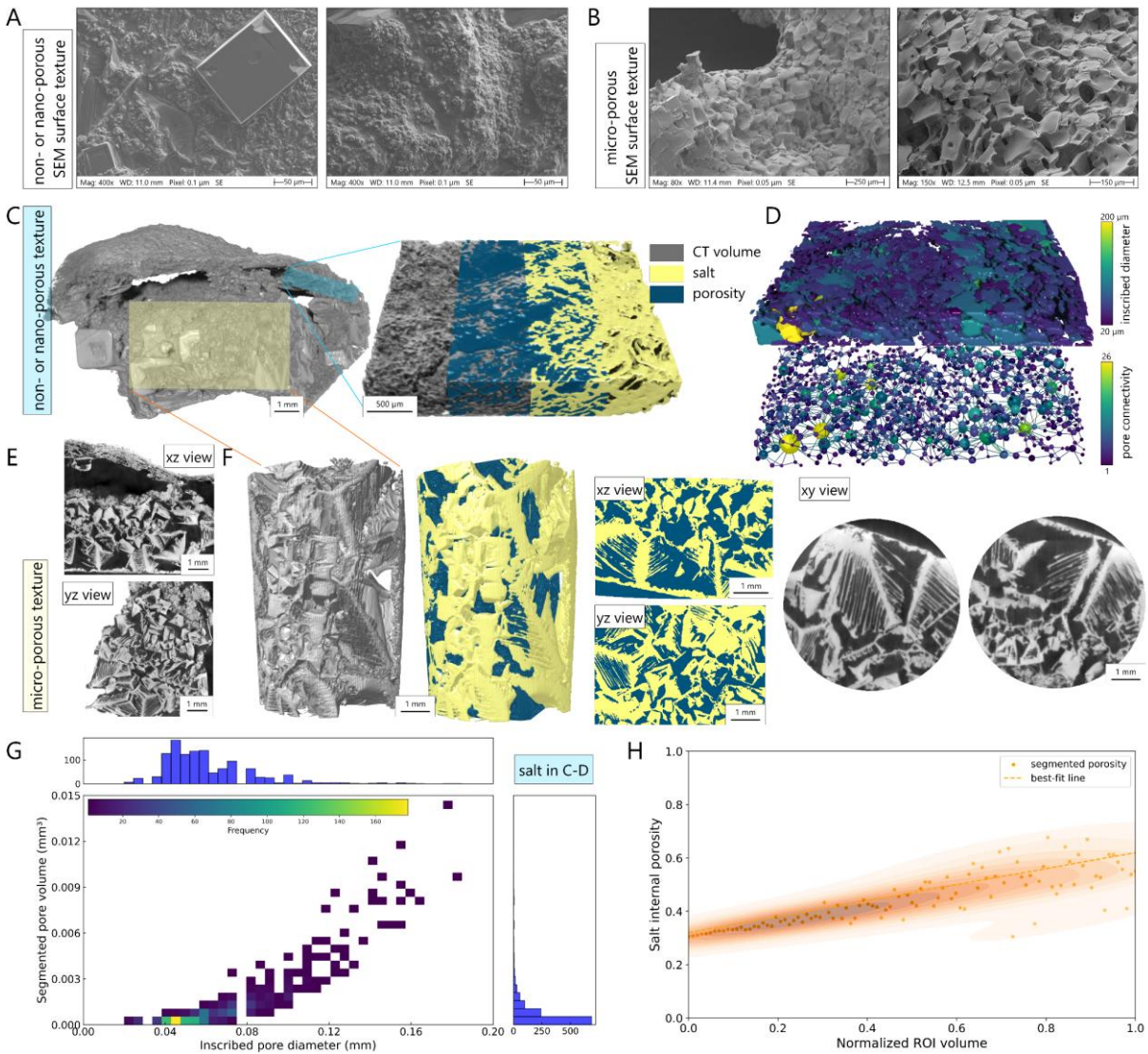


Figure 3. Texture and internal growth structure of halite precipitation. A. SEM image depicting a non-porous or nano-porous salt surface texture. B. SEM image showing micro-porous surface texture with interconnected crystals and internal pore volumes. C. X-ray tomography of a halite crystallization body where the top crust section was extracted, analyzed and segmented into salt and porosity volumes. D. Pore network extraction displaying color-coded individual pore bodies by their inscribed diameters and pore-throat maps illustrating connectivity within the porous growth structure of the extracted dense crust. E. X-ray tomography of xz and yz sections of salt body in C, visualizing the top crust and middle section of the salt body. F. Extracted cylindrical region and the corresponding segmentation of highly porous halite growth structure. G. Plot of segmented pore volume against inscribed pore diameter in the extracted salt body, displaying the frequency of different pore size ranges. H. Internal porosity plot of extracted regions of interest within X-ray tomography volumes, showing increasing internal porosity and scatter with the increase of investigation volume.

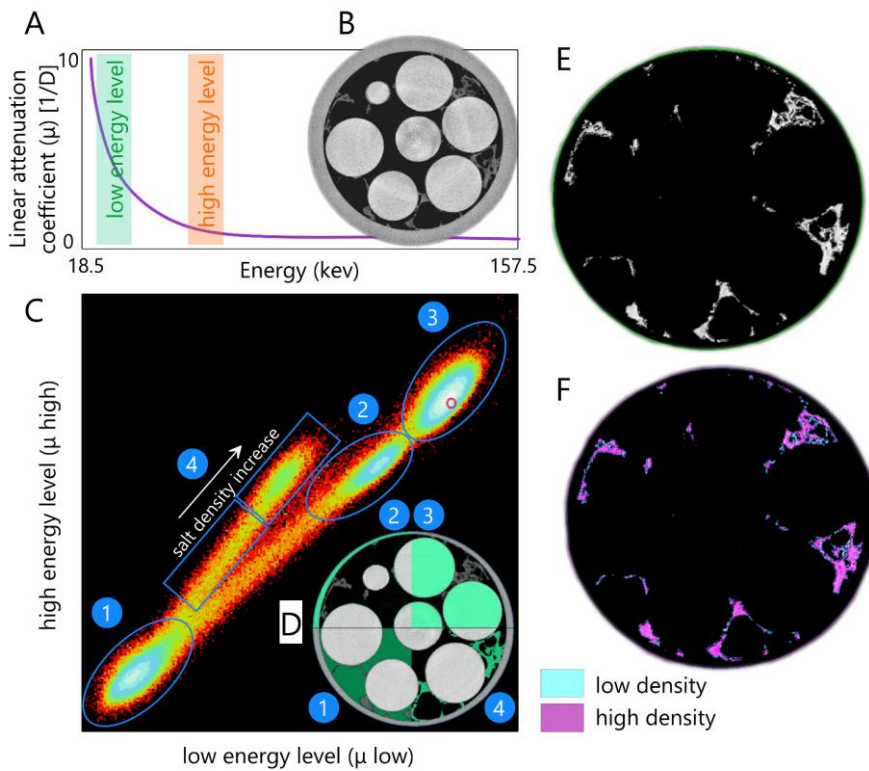


Figure 4. Spectral tomography analysis of salt precipitation. A. Measured linear attenuation coefficient (μ) plotted against the energy range and the two utilized energy levels. B. Density profile derived from multi-energy imaging. C. Dual-energy histogram crossplot of μ at high and low energy, showing distinct regions based on attenuation properties. D. Segmented image based on energy profile showing the spatial distribution of phases based on the marked regions in C. E. Halite precipitation at the given xy profile F. Profile in C where energy segmentation is incorporated and low- and high-density halite accumulations are color-coded.

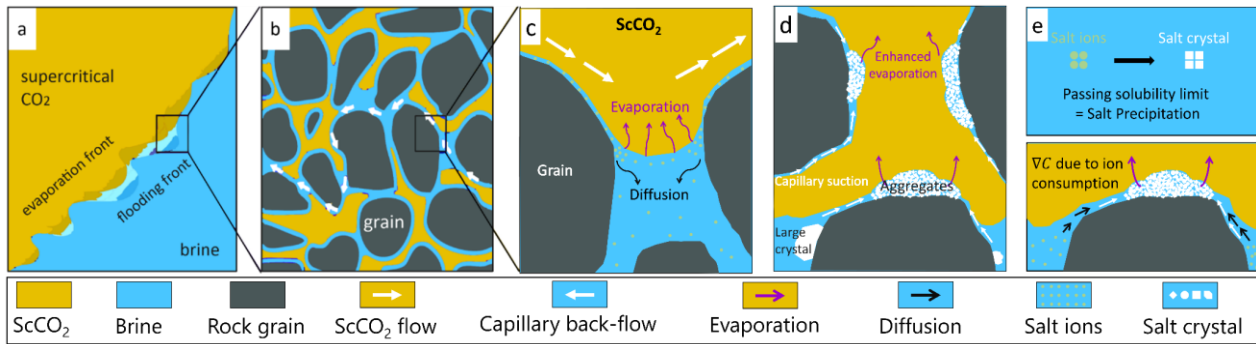


Figure 5. Principal physical mechanisms governing salt precipitation during CO₂ injection in saline aquifers: (a) two-phase viscous displacement of brine by injected CO₂, (b) capillary-driven backflow of brine toward the evaporation front, (c) evaporation-induced salt concentration and diffusion, (d) self-enhancing precipitation altering pore structure, and (e) concentration gradient from ion consumption driving diffusive flux.